Research Article

MD. Shamshuddin, Zahir Shah*, Usman, Anwar Saeed, Mansoor H. Alshehri, Narcisa Vrinceanu*, and Elisabeta Antonescu

Investigation of convective heat transport in a Carreau hybrid nanofluid between two stretchable rotatory disks

https://doi.org/10.1515/phys-2024-0078
received January 27, 2024; accepted July 28, 2024

Abstract: Hybrid nanofluids (HNFs) have outstanding energy transfer capabilities that are comparable to mono-nanofluids. Materials had appliances in obvious fields such as heat generation, micropower generation, and solar collectors. The objective of this study is to investigate the new aspects of convective heat transfer in an electrically conducting Carreau HNF situated between two parallel discs. In addition to the presumed stretchability and rotation of the discs, physical phenomena like nonlinear radiation, viscous dissipation, Joule dissipation, and heat generation and absorption are considered. The Cu and TiO_2 nanoparticles dispersed in engine oil to understand the intricate phenomenon of hybridization. The Tiwari and Das nanofluid model is employed to model the governing partial differential equations (PDEs) and then simplified using boundary layer approximation. The suitable transformations of similarity variables are defined and implemented to change the set of formulated PDEs into ordinary differential equations. The reduced system is solved semi-analytically by the homotopy analysis method. The influences of involving physical parameters on the velocity and temperature are plotted with the help of graphical figures. This study brings forth a significant contribution by uncovering novel flow features that have previously remained unexplored. By addressing a well-defined problem, our research provides valuable insights into the enhancement of thermal transport, with direct implications for diverse engineering devices such as solar collectors, heat exchangers, and microelectronics.

Keywords: heat transfer, Carreau hybrid nanofluid, Tiwari and das model, numerical simulations, stretchable and rotating disks

1 Introduction

The study of fluid flow and heat transmission in stretchy rotational discs has a broad spectrum of uses in industrial, mechanical, and thermal engineering. These applications include jet motors, spin coating, food processing, electric power generation systems, manufacturing, heat exchangers, gas turbines, medical equipment, and many others. As a result of its very valuable practical applications, researchers all over the world are actively exploring the movement of fluids and thermal exchange studies of rotating discs. The study of non-Newtonian fluid flow caused by rotating discs is an exciting and dynamic field that has piqued the interest of scientists from numerous disciplines. Non-Newtonian fluids find application across diverse industries, including paper manufacturing, petroleum extraction, and polymer sheet processing, among others. Because of the variety of non-Newtonian fluids, their behavior cannot be characterized by a single constitutive equation. Kármán [1] conducted substantial research on the fluid dynamics issue concerning rotating discs and provided a mathematical model in this context. He devised an interesting similarity transformation that converts the controlling partial differential equations

* **Corresponding author: Zahir Shah,** Department of Mathematical Sciences, University of Lakki Marwat, Lakki Marwat, 28420, Khyber Pakhtunkhwa, Pakistan, e-mail: Zahir@ulm.edu.pk
* **Corresponding author: Narcisa Vrinceanu,** Department of Industrial Machines and Equipments, Faculty of Engineering, "Lucian Blaga" University of Sibiu, 10 Victoriei Boulevard, Sibiu, Romania, e-mail: vrinceanu.narcisai@ulbsibiu.ro
MD. Shamshuddin: Department of Mathematics, School of Computer Science and Artificial Intelligence, SR University, Warangal-506371, Telangana, India
Usman: School of Qilu Transportation, Shandong University, Jinan, China; Department of Computer Science, National University of Sciences and Technology, Balochistan Campus (NBC), Quetta, 87300, Pakistan
Anwar Saeed: Department of Mathematic, Abdul Wali Khan University Mardan, Mardan, Khyber Pakhtunkhwa, Pakistan
Mansoor H. Alshehri: Department of Mathematics, College of Science, King Saud University, P.O. Box 2455, Riyadh, 11451, Saudi Arabia
Elisabeta Antonescu: Preclinical Department, Faculty of Medicine, Lucian Blaga University of Sibiu, Sibiu, 550024, Romania

(PDEs) to ordinary differential equations (ODEs). These ODEs are then resolved numerically using the momentum integral approach, allowing for more efficient system analysis. Von Karman's work has established a solid foundation for understanding and investigating the intricate fluid dynamics and heat transport in spinning disc systems. Fang and Zhang [2] accomplished a great feat by getting the correct solution to the Navier–Stokes equations for a fluid flowing between two infinitely flexible discs undergoing stretching velocity acceleration. Imtiaz *et al.* [3] investigated the effect of single and multiwall carbon nanotubes on the flow and heat transmission between two spinning and stretching discs in great detail. Ahmed *et al.* [4] proposed a novel mathematical model to investigate the behavior of an electrically conductive Maxwell fluid. This fluid flows between two axially aligned rotating and stretching discs, keeping their spacing constant. Usman *et al.* [5] researched on increasing heat transport within a blood nanofluid. They used the power-law model to investigate the effect of a heat source/sink in the presence of two revolving stretchable discs to promote the heat transfer process. Usman *et al.* [6] explored the three-dimensional heat transfer and liquid flow processes that occur within a Carreau liquid contained between rotating stretchy discs. Important advances in the study of nanofluid flow over a variety of geometries were made by Das and Ali [7,8]. Yashkun *et al.* [9] scrutinized the heat transmission characteristics of magnetohydrodynamic (MHD) hybrid nanofluids (HNFs) on shrinking and stretching surfaces, taking into account the effects of suction and thermal radiation. Lund *et al.* [10] studied the effect of Joule heating and viscous dissipation on unsteady MHD 2D flow over a constantly parallel regular shrinking sheet.

In the past few years, scientists have been actively looking for new fluids to replace nanofluids and attain highly efficient heat transfer capacities. This pursuit has given rise to the phrase "hybrid nanofluids (HNFs)." By integrating two distinct nanoparticle variants into a foundational fluid, these novel fluids go beyond traditional nanofluids. When compared to ordinary nanofluids, the addition of numerous nanoparticles in HNFs results in superior thermal augmentation. Waini *et al.* [11], for example, investigated the impact of Cu–Al_2O_3–water HNF flow and heat transmission along a leaky moving sheet. In terms of increasing heat transfer qualities, their findings indisputably proved that HNFs outperform nanofluids having only a single type of nanoparticle. This growing interest in HNFs highlights its potential as a cost-effective solution for a wide array of applications involving heat transfer. Zainal *et al.* [12] explored mixed convection flow in an HNF across a vertical flat plate under the effect of MHD and convective boundary conditions. Their research found dual solutions in both the aiding and opposing flow areas. Waini *et al.* [13] investigated the consistent movement of HNF with mixed convection over a porous vertical plane. Within a given range of buoyancy factors, they discovered numerous dual solutions. Furthermore, the introduction of hybrid nanoparticles was discovered to slow down boundary layer separation. Rostami *et al.* [14] investigated sustained laminar MHD-mixed convection stagnation point flow in an HNF across a vertical permeable flat plate. They discovered two distinct solutions within a specified range of the buoyancy parameter and performed stability tests on these solutions. Shamshuddin *et al.* [15] examined the flow of HNF across a spinning surface and the effects of entropy formation. Farooq *et al.* [16] investigated the electromagnetic flow of HNF between two discs. The impacts of entropy formation on the flow of HNF across discs were investigated by Agrawal and Kaswan [17]. Waini *et al.* [18] used a Cu–Al_2O_3–water HNF to evaluate the unsteady flow and heat transport toward a shrinking–stretching surface. They discovered that as the suction parameter was increased, the velocity of the HNF increased. Furthermore, they revealed that the employment of the HNF, together with the stimulus of the suction force, resulted in an additional temperature reduction. Khashi'ie *et al.* [19] explored the outcome of convective circumstances and velocity slip on the 3D flow of HNF over a surface undergoing stretching and shrinking numerically. Increasing the Biot and slip parameters boosted heat transfer rates, whereas growing the Cu solid volume fraction had the reverse impact. Anuar *et al.* [20] investigated the stimulus of boundary layer flow and heat transmission over an inclined leaky surface that undergoes both stretching and shrinking, utilizing an HNF composed of Ag–MgO–water. They discovered that increasing the angle of inclination and suction parameters increased the local Nusselt number. Furthermore, increasing the volume percentage of Ag nanoparticles in the MgO–water nanofluid resulted in a decrease in the local Nusselt number.

Non-Newtonian fluids have gained a lot of interest in the industrial world because of their diverse applications. Much experimental and theoretical research has been conducted to better understand the transport behavior of these fluids, which are important in a variety of genetic and industrial processes, materials, and mechanical engineering. Non-Newtonian liquids can be found in a wide range of materials, including biomedical fluxes, splashes, bio-fluids in genetic material, and polymers. Despite extensive study in this field, many researchers continue to investigate non-Newtonian fluids from diverse angles, resulting in countless publications [21–23]. The well-designed Carreau fluid model [24] stands out among the constitutive models developed to represent the features of shear thinning/thickening non-Newtonian liquids. Sulochana *et al.* [25], for example, used the Runge–Kutta method in conjunction with a shooting operation to quantitatively

analyze the effect of a stagnation point on the Carreau nanofluid. The magnetic parameter had a considerable influence on the flow field according to their findings. Khan *et al.* [26] recently proposed a new model for the three-dimensional flow of Carreau fluid that incorporates nonlinear thermal radiation. Irfan *et al.* [27] explored the 3D flow of Carreau fluid in more detail, taking into account numerous additional features. The thermal Biot number, Brownian motion, thermophoresis, and thermal radiation characteristics all had substantial effects on the temperature field, according to their research. Rooman *et al.* [28] investigated the heat transfer characteristics of Carreau nanofluid in the context of the renal tubule. There are many emerging streams that are associated with the different materials used in engineering science technology, which includes studies such as thermoelastic interaction in functional graded material [29], photo-thermal interactions in a semi-conductor material [30], and prothermal elastic materials [31].

This current analysis effort intends to analyze the importance of nonlinear radiation, heat, and Joule dissipation effects in the act of the phenomenon of surface heating by parallel rotatory disk in the presence of an HNF. By investigating the behavior of Cu and TiO_2 nanoparticles dispersed in water, we aim to understand the intricate phenomenon of hybridization. This current novelty is to put effort to analyzing the importance of nonlinear radiation, heat, and Joule dissipation effects in the act phenomenon of surface heating by parallel rotatory disk in the presence of HNF.

2 Formulation of the problem

The following assumptions are made while formulating the problem:

- Consider a 3D flow of the Carreau HNF flow between two parallel, rotating, and stretching discs, where the bottom disc is set at $z = 0$ and the upper disc is set at $z = h$.
- The presumed axial-symmetric flow, which distributes radially on the discs and is electrically conducting, strikes them at a 90° angle.
- The bottom and upper discs are rotating at a rate of rs_1, rs_2 and stretching at a rate of $r\Omega_1$, $r\Omega_2$, respectively.
- The constant magnetic field while preserving B_0's strength is applied perpendicular to the rotating discs.
- The axial-symmetric flow assumes that the pressure is constant and eliminates any fluctuation with respect to θ^*.
- Under nonlinear radiation and heat generation/absorption concerning convective boundary conditions, the phenomena of heat transfer are examined.
- In addition, T_1 and T_2 stand for the temperatures of the lower and top discs, respectively (Figure 1).

The leading PDEs of motion and energy for the time-independent 3D flow of a hybrid Carreau nanofluid between two stretchable spinning discs following Usman *et al.* [5], while taking into account viscous dissipation and joule heating due to convective heat transfer are expressed as follows:

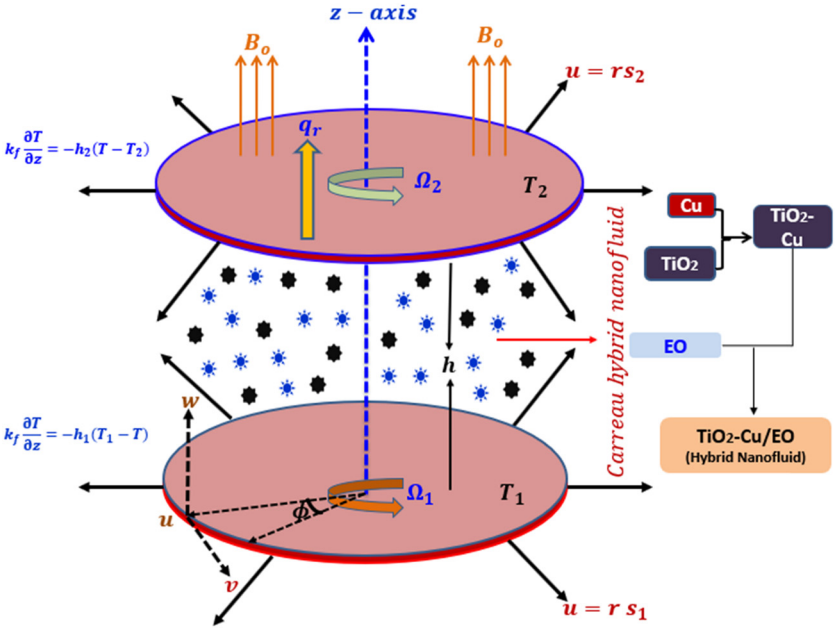

Figure 1: Flow configuration of magnetized Carreau HNF.

$$\frac{\partial u}{\partial r} + \frac{u}{r} + \frac{\partial w}{\partial z} = 0, \tag{1}$$

$$\left.\begin{aligned} u\frac{\partial u}{\partial r} - \frac{v^2}{r} + w\frac{\partial u}{\partial z} &= \upsilon_{\mathrm{hnf}}\left(\frac{\partial^2 u}{\partial z^2}\right)\left\{1 + \Gamma^2\left(\frac{\partial u}{\partial z}\right)^2\right\}^{\frac{n-1}{2}} \\ &+ \upsilon_{\mathrm{hnf}}(n-1)\Gamma^2\left(\frac{\partial u}{\partial z}\right)^2\left(\frac{\partial^2 u}{\partial z^2}\right)\left\{1 + \Gamma^2\left(\frac{\partial u}{\partial z}\right)^2\right\}^{\frac{n-3}{2}} - \frac{\sigma_{\mathrm{hnf}}B_0^2}{\rho_{\mathrm{hnf}}}u, \end{aligned}\right\} \tag{2}$$

$$\left.\begin{aligned} u\frac{\partial v}{\partial r} + \frac{uv}{r} + w\frac{\partial v}{\partial z} &= \upsilon_{\mathrm{hnf}}\left(\frac{\partial^2 v}{\partial z^2}\right)\left\{1 + \Gamma^2\left(\frac{\partial v}{\partial z}\right)^2\right\}^{\frac{n-1}{2}} \\ &+ \upsilon_{\mathrm{hnf}}(n-1)\Gamma^2\left(\frac{\partial u}{\partial z}\right)^2\left(\frac{\partial^2 u}{\partial z^2}\right)\left\{1 + \Gamma^2\left(\frac{\partial u}{\partial z}\right)^2\right\}^{\frac{n-3}{2}} - \frac{\sigma_{\mathrm{hnf}}B_0^2}{\rho_{\mathrm{hnf}}}v, \end{aligned}\right\} \tag{3}$$

$$\left.\begin{aligned} u\frac{\partial T}{\partial r} + w\frac{\partial T}{\partial z} &= \alpha_{\mathrm{hnf}}\frac{\partial^2 T}{\partial z^2} + \frac{16\sigma^*}{3k^*(\rho c_{\mathrm{p}})_{\mathrm{hnf}}}\frac{\partial}{\partial z}\left(T^3\frac{\partial T}{\partial z}\right) \\ &+ \frac{\mu_{\mathrm{hnf}}}{(\rho c_{\mathrm{p}})_{\mathrm{hnf}}}\left[\left(\frac{\partial u}{\partial z}\right)^2 + \left(\frac{\partial v}{\partial z}\right)^2\right] \\ &+ \frac{\sigma_{\mathrm{hnf}}B_0^2}{(\rho c_{\mathrm{p}})_{\mathrm{hnf}}}(u^2 + v^2) + \frac{Q_0}{(\rho c_{\mathrm{p}})_{\mathrm{hnf}}}(T - T_2). \end{aligned}\right\} \tag{4}$$

The boundary conditions are as given as follows:

$$\left.\begin{aligned} &u = rs_1,\ \ v = r\Omega_1,\ \ w = 0,\ \ k_{\mathrm{f}}\frac{\partial T}{\partial z} = -h_1(T_1 - T), \\ &\text{at } z = 0, \\ &u = rs_2,\ \ v = r\Omega_2,\ \ w = 0,\ \ k_{\mathrm{f}}\frac{\partial T}{\partial z} = -h_2(T - T_2), \\ &\text{at } z = h. \end{aligned}\right\} \tag{5}$$

2.1 Hybrid nanomaterial properties

The thermophysical characteristics and relation of nano and hybrid nanomaterials are presented in Tables 1 and 2, respectively.

2.1.1 Similarity transformation

The similarity parameters for the current issue can be characterized as follows:

$$\left.\begin{aligned} &\eta = z\sqrt{\frac{\Omega_1}{\upsilon_{\mathrm{f}}}}, u = r\Omega_1 F(\eta),\ \ v = r\Omega_1 G(\eta), \\ &w = \sqrt{\Omega_1\upsilon_{\mathrm{f}}}H(\eta),\ \ \theta(\eta) = \frac{T - T_2}{T_1 - T_2}. \end{aligned}\right\} \tag{6}$$

By introducing (6) into (1)–(5), we achieved the ODEs:

$$H' + 2F = 0, \tag{7}$$

Table 1: Experimental values of engine oil, Cu, and TiO_2 [32]

	ρ(kg/m^3)	c_{p}(J/kg K)	k(W/m K)	σ (Ω m)$^{-1}$
Engine oil (EO)	884	1910	0.1440	5.5×10^{-6}
Copper (Cu)	8,933	385.0	401.0	5.96×10^{-8}
Titanium dioxide (TiO_2)	4,250	686.20	8.9538	6.27×10^{-5}

$$\left.\begin{aligned} F^2 - G^2 + F'H &= \frac{A_2}{A_1}F''\{1 + \mathrm{We}^2F'^2\}^{\frac{n-1}{2}} + \frac{A_2}{A_1}(n-1) \\ &\times \mathrm{We}^2F'^2F''\{1 + \mathrm{We}^2F'^2\}^{\frac{n-3}{2}} - \frac{A_3}{A_1}MF, \end{aligned}\right\} \tag{8}$$

$$\left.\begin{aligned} 2FG + HG' &= \frac{A_2}{A_1}G''\{1 + \mathrm{We}^2G'^2\}^{\frac{n-1}{2}} + \frac{A_2}{A_1}(n-1) \\ &\times \mathrm{We}^2G'^2G''\{1 + \mathrm{We}^2G'^2\}^{\frac{n-3}{2}} - \frac{A_3}{A_1}MG, \end{aligned}\right\} \tag{9}$$

$$\left.\begin{aligned} \mathrm{Pr}H\theta' &= \frac{A_5}{A_4}\theta'' + \frac{4\mathrm{Rd}}{3A_4}\{(1 + (\theta_{\mathrm{w}} - 1)\theta)^3\theta'\}' \\ &+ \frac{A_2}{A_4}\mathrm{PrEc}(F'^2 + G'^2) + \frac{A_3}{A_4}\mathrm{PrEc}M(F^2 + G^2) \\ &+ \frac{\mathrm{Pr}Q^*}{A_4}\theta. \end{aligned}\right\} \tag{10}$$

The transformed boundary constraints are presented by

$$\left.\begin{aligned} &F(0) = A,\ \ G(0) = 1,\ \ H(0) = 0, \\ &\theta'(0) = -C(1 - \theta(0)), \\ &F(1) = B,\ \ G(1) = \Omega,\ \ H(1) = 0,\ \ \theta'(1) = -D\theta(1). \end{aligned}\right\} \tag{11}$$

In this case, the dimensionless emergent parameters are specified as follows:

$$\left.\begin{aligned} &A_1 = \frac{\rho_{\mathrm{hnf}}}{\rho_{\mathrm{f}}},\ A_2 = \frac{\mu_{\mathrm{hnf}}}{\mu_{\mathrm{f}}},\ A_3 = \frac{\sigma_{\mathrm{hnf}}}{\sigma_{\mathrm{f}}},\ A_4 = \frac{(\rho c_{\mathrm{p}})_{\mathrm{hnf}}}{(\rho c_{\mathrm{p}})_{\mathrm{f}}}, \\ &A_5 = \frac{k_{\mathrm{hnf}}}{k_{\mathrm{f}}},\ M = \frac{B_0^2\sigma_{\mathrm{f}}}{\Omega_1\rho_{\mathrm{f}}},\ A = \frac{s_1}{\Omega_1},\ B = \frac{s_2}{\Omega_1},\ \Omega = \frac{\Omega_2}{\Omega_1}, \\ &\mathrm{We} = \frac{\Omega_1^{\frac{3}{2}}r\Gamma}{\sqrt{\upsilon_{\mathrm{f}}}},\ \mathrm{Ec} = \frac{r^2\Omega_1^2}{(\rho c_{\mathrm{p}})_{\mathrm{f}}(T_1 - T_2)}, \\ &\mathrm{Pr} = \frac{\upsilon_{\mathrm{f}}}{\alpha_{\mathrm{f}}},\ \mathrm{Rd} = \frac{4\sigma^*T_\infty^3}{k_{\mathrm{f}}k^*},\ \theta_{\mathrm{w}} = \frac{T_1}{T_2},\ Q^* = \frac{Q_0}{(\rho c_{\mathrm{p}})_{\mathrm{f}}\Omega_1}, \\ &C = \frac{h_1}{k_{\mathrm{f}}}\sqrt{\frac{\upsilon_{\mathrm{f}}}{\Omega_1}},\ D = \frac{h_2}{k_{\mathrm{f}}}\sqrt{\frac{\upsilon_{\mathrm{f}}}{\Omega_1}}, \end{aligned}\right\} \tag{12}$$

where A_1, A_2, A_3, A_4, A_5 are constants. M, A, B, Ω, We, Ec, Pr, Rd, θ_{w}, Q^*, C and D are the magnetic field parameter, stretching parameters, Weissenberg number, rotation parameter, Eckert number, Prandtl number, radiation

Table 2: Nano and hybrid nanofluids' thermo-physical interactions [32]

Properties	Nano and hybrid
Viscosity	$\frac{\mu_{hnf}}{\mu_{bf}} = \frac{1}{(1-\phi_{Cu}-\phi_{TiO_2})^{2.5}}$
Density	$\frac{\rho_{hnf}}{\rho_{bf}} = \phi_{Cu}\left(\frac{\rho_{Cu}}{\rho_{bf}}\right) + \phi_{TiO_2}\left(\frac{\rho_{TiO_2}}{\rho_{bf}}\right) + (1-\phi_{Cu}-\phi_{TiO_2})$
Thermal capacity	$\frac{(\rho c_p)_{hnf}}{(\rho c_p)_{bf}} = \phi_{Cu}\left(\frac{(\rho c_p)_{Cu}}{(\rho c_p)_{bf}}\right) + \phi_{TiO_2}\left(\frac{(\rho c_p)_{Cu}}{(\rho c_p)_{bf}}\right) + (1-\phi_{Cu}-\phi_{TiO_2})$
Thermal conductivity	$\frac{k_{hnf}}{k_{bf}} = \frac{\frac{(\phi_{Cu}k_{Cu}+\phi_{TiO_2}k_{TiO_2})}{\phi_{Cu}+\phi_{TiO_2}} + \left\{2k_{bf} + 2(\phi_{Cu}k_{Cu}+\phi_{TiO_2}k_{TiO_2}) - 2(\phi_{Cu}+\phi_{TiO_2})k_{bf}\right\}}{\frac{(\phi_{Cu}k_{Cu}+\phi_{TiO_2}k_{TiO_2})}{\phi_{Cu}+\phi_{TiO_2}} + \left\{2k_{bf} - (\phi_{Cu}k_{Cu}+\phi_{TiO_2}k_{TiO_2}) + (\phi_{Cu}+\phi_{TiO_2})k_{bf}\right\}}$
Electrical conductivity	$\frac{\sigma_{hnf}}{\sigma_{bf}} = \frac{\frac{(\phi_{Cu}\sigma_{Cu}+\phi_{TiO_2}\sigma_{TiO_2})}{\phi_{Cu}+\phi_{TiO_2}} + \left\{2\sigma_{bf} + 2(\phi_{Cu}\sigma_{Cu}+\phi_{TiO_2}\sigma_{TiO_2}) - 2(\phi_{Cu}+\phi_{TiO_2})\sigma_{bf}\right\}}{\frac{(\phi_{Cu}k_{Cu}+\phi_{TiO_2}k_{TiO_2})}{\phi_{Cu}+\phi_{TiO_2}} + \left\{2\sigma_{bf} - (\phi_{Cu}\sigma_{Cu}+\phi_{TiO_2}\sigma_{TiO_2}) + (\phi_{Cu}+\phi_{TiO_2})\sigma_{bf}\right\}}$

parameter, surface heating parameter, heat generation/absorption parameter, and lower and upper disk parameters.

2.2 Physically interesting quantities

2.2.1 Surface drag forces

The surface drag forces or skin friction coefficients at the heated surface are defined as follows in radial and azimuthal directions:

$$C_{Fr} = \frac{\tau_{rz}}{\rho_f(cr)^2}, \quad C_{G\theta^*} = \frac{\tau_{G\theta^*}}{\rho_f(cr)^2}\Bigg\}, \tag{13}$$

where τ_{wr} and $\tau_{w\theta^*}$ are radial and azimuthal direction shear stresses, respectively, which are specified by:

$$\left.\begin{aligned}\tau_{rz} &= \mu_{hnf}\left[\left(\frac{\partial u}{\partial z}\right)\left\{1+\Gamma^2\left(\frac{\partial u}{\partial z}\right)^2\right\}^{\frac{n-1}{2}}\right]_{z=0},\\ \tau_{\theta^* z} &= \mu_{hnf}\left[\left(\frac{\partial v}{\partial z}\right)\left\{1+\Gamma^2\left(\frac{\partial v}{\partial z}\right)^2\right\}^{\frac{n-1}{2}}\right]_{z=0}.\end{aligned}\right\} \tag{14}$$

By applying (6), the dimensionless skin friction coefficient is reduced as follows:

$$\left.\begin{aligned}\mathrm{Re}^{\frac{1}{2}}C_{Fr} &= A_2F'(0)[1+\mathrm{We}^2(F'(0))^2]^{\frac{n-1}{2}},\\ \mathrm{Re}^{\frac{1}{2}}C_{G\theta^*} &= A_2G'(0)[1+\mathrm{We}^2(G'(0))^2]^{\frac{n-1}{2}}.\end{aligned}\right\} \tag{15}$$

2.2.2 Heat transfer rate

The heat transfer rate, or local Nusselt number, or temperature gradient is denoted as follows:

$$\mathrm{Nu}_r = \frac{rq_w}{k_f(T_1-T_2)}\Bigg\}. \tag{16}$$

Here, q_w is the heat flux and is described as follows:

$$q_w = \left[-k_{hnf}\frac{\partial T}{\partial z} + (q_r)_w\right]_{z=0}\Bigg\}. \tag{17}$$

The nondimensional will lead to

$$\mathrm{Re}^{-\frac{1}{2}}\mathrm{Nu}_r = -A_5[\{1+\mathrm{Rd}(1+(\theta_w-1)\theta(\eta))^3\}\theta'(\eta)]_{\eta=0}\Bigg\}, \tag{18}$$

where $\mathrm{Re}_r = \frac{\Omega_1 r^2}{\upsilon_f}$ is the local Reynolds number.

3 Homotopy analysis method (HAM) solution

The initial guesses are defined as follows:

$$\left.\begin{aligned}f_0(\eta) &= A(1-\eta)+b\eta, \quad f_0(\eta) = 1-\Omega\eta^2,\\ \theta_0(\eta) &= \frac{C+CD}{C+D+CD}(1-\eta).\end{aligned}\right\} \tag{19}$$

The linear operators are defined as follows:

$$L_f = f''(\eta) - f(\eta), \quad L_g = g''(\eta) - g(\eta), \quad L_\theta = \theta''(\eta) - \theta(\eta), \tag{20}$$

with properties:

$$L_f(C_1 + C_2\eta) = 0, \quad L_g(C_3 + C_4\eta) = 0, \quad L_\theta(C_5 + C_6\eta) = 0, \tag{21}$$

where C_1–C_6 are the constants of the general solution. Detailed procedures performed relying on the framework can be seen in the study by Lone *et al.* [33].

3.1 Convergence analysis

The HAM technique is the most useful technique for the solution of nonlinear higher-order boundary value problems. The auxiliary parameter $\hbar_f$ plays a vital role in calculating the convergence region of the series solutions of a boundary value problem. Here, the auxiliary parameters $\hbar_f$, $\hbar_g$, and $\hbar_\theta$ are calculated for the modeled problem as shown in Figure 2. From this figure, we see that the convergence region for the axial velocity profile is $-1.85 \le \hbar_f \le 0.23$, radial velocity profile is $-2.00 \le \hbar_g \le 0.25$, and temperature profile is $-1.00 \le \hbar_\theta \le 0.23$.

3.2 Validation

Table 3 reveals the comparison of computed results of the current investigation with previously reported cases in the study by Irfan *et al.* [34] keeping We = $Q^* = 0, n = 3$ as particularized in table. The comparative results showed a strong level of consistency and were in good agreement, which is strong support for the validity and dependability of the present findings. We can thus say with confidence that the method developed for examining the flow of Carreau HNF is highly trustworthy and may be used with considerable confidence.

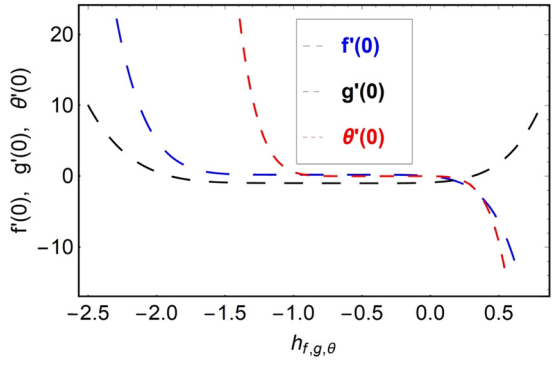

Figure 2: h curves for the function f, g, θ.

Table 3: Computed values of $\mathrm{Re}^{-\frac{1}{2}}\mathrm{Nu}_r$ compared to some limiting cases when We = $Q^* = 0, n = 3$

Pr	Irfan *et al.* [34]	Present results
0.7	0.45445767	0.454458
1.0	0.58201280	0.582013
1.3	0.69302203	0.693022
1.6	0.79227119	0.792272
1.8	0.85344101	0.853441
2.0	0.91134742	0.911348
5.0	1.56806380	1.568063
7.0	1.89542450	1.895425
10.0	2.30801360	2.308014
20.0	3.35396200	3.353962
70.0	6.46238930	6.462390

4 Results and discussion

A time-independent 3D model for Carreau HNF between two parallel, rotating, and stretching discs is generated. It is important to mention that two types of nanoparticles are imposed in the suspension of engine oil. Mechanisms of nonlinear radiation, heat, and Joule dissipation are implemented in the heat energy mechanism. Such a complex model is solved using a semi-analytical scheme called HAM. Detailed discussions regarding thermal and velocity profiles are mentioned in the following sections.

4.1 Velocity profiles

The velocity profiles are graphed using the dimensionless similarity variable η to anticipate the responses of fluids exhibiting shear-thinning behavior with $n = 0.5$ and fluids showing shear-thickening behavior with $n = 1.5$.

Figures 3 and 4 show the effect of radial and azimuthal velocities for different values of the stretching parameter at the lower disc (denoted as A). When the stretching rate parameter A of the lower disc increases in stretchable rotatory discs, it has significant effects on the velocity profiles along the radial and tangential directions. As the bottom disk's stretching rate parameter A increases, the material in the radial direction suffers more dramatic stretching or expansion. This expansion makes more room for the fluid to flow outward in a radial direction. As a result of the

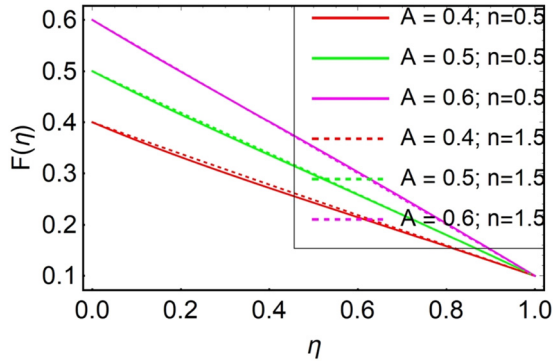

Figure 3: Influence of A and n on $F(\eta)$.

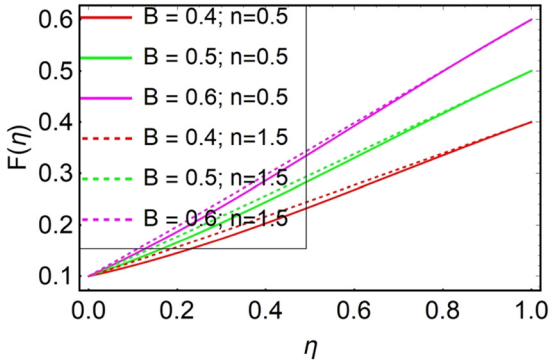

Figure 5: Influence of B and n on $F(\eta)$.

increased volume available for fluid passage, the fluid's velocity increases along the radial path. In contrast, increasing the stretching rate parameter A can result in tangential contraction or a reduction in the azimuthal dimension of the bottom disc. This azimuthal contraction influences fluid flow along the azimuthal direction, resulting in a drop in velocities along this path. Changes in the dimensions of the lower disc have an effect on the overall flow patterns in the system. Increased radial expansion and azimuthal contraction can cause flow patterns to shift, potentially resulting in lower azimuthal velocities and increased radial velocities.

Figures 5 and 6 show the effect of radial and azimuthal velocities for different values of the stretching parameter at the upper disc (denoted as B). When the stretching rate parameter B of the upper disc increases in the setting of stretchable rotatory discs, it causes distinct changes in the velocity profiles along the radial and tangential directions. An increase in the stretching rate parameter B results in increased radial stretching or expansion of the material. This radial expansion allows more fluid to flow away from the center of rotation. As a result of the increased volume available for fluid movement, the fluid's velocity increases in the radial direction. The increased stretching of the top disc along the azimuthal direction causes azimuthal contraction or dimension decrease. The fluid flow within the disc is affected by this azimuthal contraction, resulting in a drop in velocities along the azimuthal direction. The changes in dimensions caused by increasing the stretching rate parameter B have an effect on the overall flow patterns inside the system. The observed drop in velocities along the azimuthal direction and rise in velocities along the radial

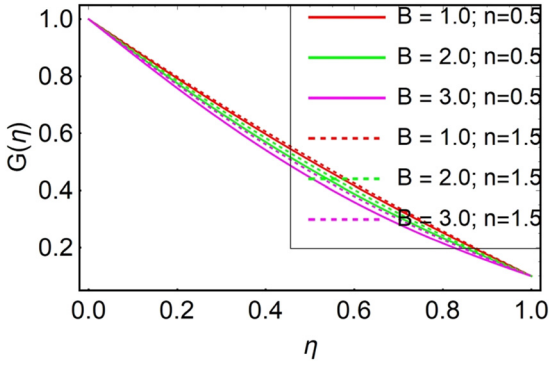

Figure 6: Influence of B and n on $G(\eta)$.

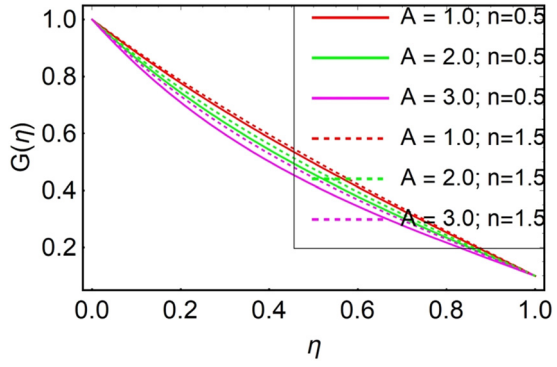

Figure 4: Influence of A and n on $G(\eta)$.

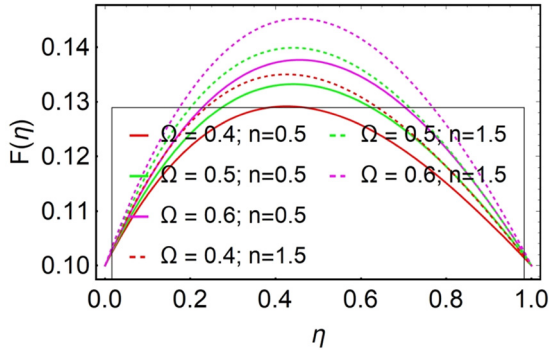

Figure 7: Influence of Ω and n on $F(\eta)$.

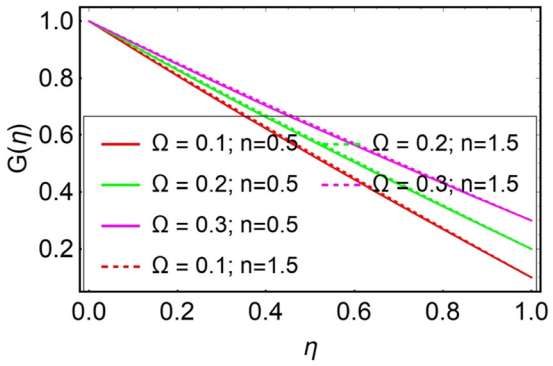

Figure 8: Influence of Ω and n on $G(\eta)$.

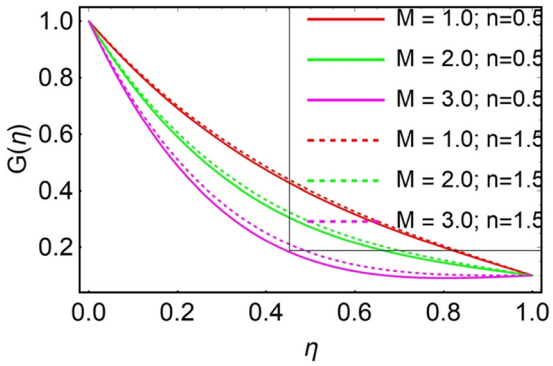

Figure 10: Influence of M and n on $G(\eta)$.

direction may be due to variations in flow patterns caused by radial expansion and azimuthal contraction.

Figures 7 and 8 depict the influence of radial and azimuthal velocities, respectively, for varying values of the rotation parameter (designated as Ω). The rotation parameter Ω has a considerable influence on the fluid flow behavior in the context of stretchy rotatory discs. When the rotation parameter increases, the rotational speed or angular velocity of the disc increases. This increase in rotational speed has a number of consequences on the fluid flow within the disc. As the rotational speed of the disc increases, so does the centrifugal force experienced by the fluid. This force pulls the fluid outward in the radial direction, resulting in larger radial velocities. The greater the centrifugal force, the faster the fluid moves away from the center of the revolution. The circular path around the center of rotation corresponds to the tangential direction. When the rotation parameter is increased, the disc spins faster, and this increased rotational speed transfers more kinetic energy to the fluid particles. As a result, the fluid particles in the tangential direction gain speed, increasing the tangential velocity. The impacts of n = 0.5 and n = 1.5 exhibit nearly comparable outcomes.

Figure 9 and 10 depict the influence of radial and azimuthal velocities, respectively, for varying values of the magnetic parameter (designated as M). The velocity profiles in stretchy rotatory discs decrease noticeably when the magnetic parameter increases in both the radial and tangential directions. In stretchable rotatory disks, the influence of a magnetic field affects the flow behavior of the fluid. The magnetic forces applied to the fluid grow more prominent as the magnetic parameter is increased. These forces interact with the fluid's motion, causing velocities to decrease in both the radial and tangential directions. Simply put, when the magnetic parameter increases, so do the magnetic forces, which impede fluid movement in the radial and tangential directions. As a result, velocities in these directions are slower than in situations with less magnetic impact. Furthermore, the enhancement of viscous and Joule dissipation, thickening of the boundary layer, modifications in flow structure, and Lorentz force acting as a magnetic drag are the main causes of the decrease in radial and azimuthal velocities with increasing magnetic parameter. These effects combined lead to the suppression of fluid motion in the presence of a strong magnetic field. The impacts of n = 0.5 and n = 1.5 exhibit nearly comparable outcomes.

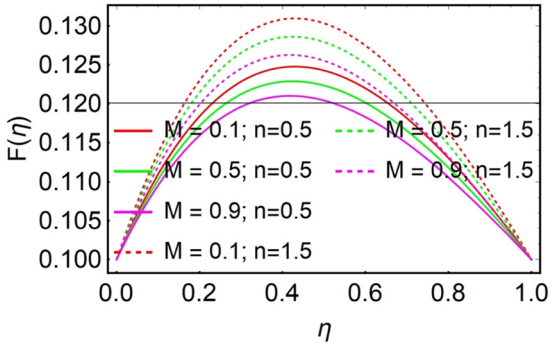

Figure 9: Influence of M and n on $F(\eta)$.

4.2 Temperature profiles

Figure 11 depicts the effect of the Biot number at lower disc parameter C on the nondimensional temperature distribution. When the temperature ratio (θ_w) is 1 (showing equal temperatures in both regions) and the Biot number at the lower disc parameter C increases, convective heat transfer at the surface is more effective than internal heat conduction within the solid. At θ_w = 1, where the temperatures are the same in both locations, an increase in the Biot number indicates that convective heat transfer is

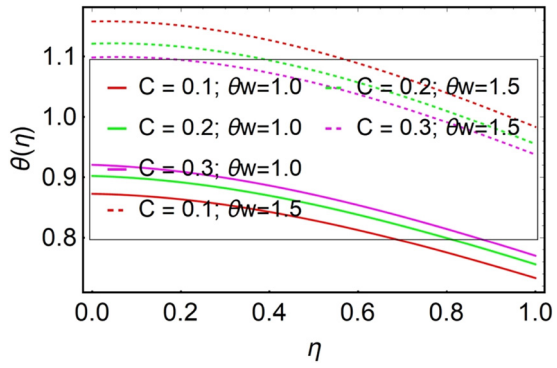

Figure 11: Influence of C and θ_w on $\theta(\eta)$.

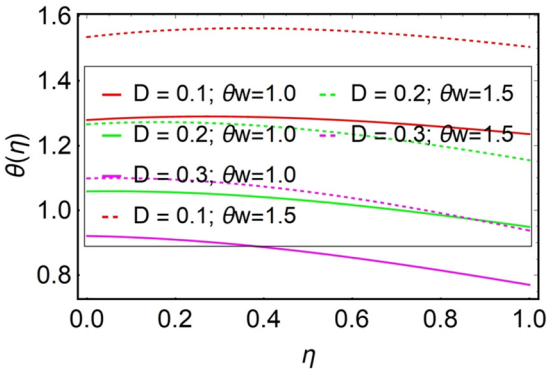

Figure 12: Influence of D and θ_w on $\theta(\eta)$.

becoming more important relative to internal heat conduction. Improved convective heat transfer promotes improved heat exchange between the solid and the surrounding fluid. As a result, the temperature profiles in this situation rise faster because heat is transported more efficiently from the solid to the fluid. When the temperature ratio (θ_w) is 1.5 (showing a temperature difference between the regions) and the Biot number at the lower disc parameter C rises, it indicates that convective heat transfer is becoming more important in comparison to internal heat conduction within the solid. At $\theta_w = 1.5$, the higher temperature in one part compared to the other produces a temperature gradient, which causes heat transfer from the hotter to the colder region. A higher Biot number, indicating greater convective heat transfer, would result in more effective heat exchange between the solid and the surrounding fluid. Because of the improved convection, the heat is transferred away from the solid more effectively, resulting in a decrease in temperature profiles. It is also noted that when the temperature ratio parameter θ_w increases, the temperature profile also increases because heat naturally flows from higher-temperature regions to lower-temperature regions. The pushing power for heat transmission grows as the temperature difference between two places increases. As a result, more heat moves from the hotter to the cooler zone.

Figure 12 depicts the effect of the Biot number at upper disc parameter D on the nondimensional temperature distribution. When the Biot number at the upper disc parameter D in stretchy rotatory discs increases at both $\theta_w = 1$ and $\theta_w = 1.5$, the temperature profiles fall due to increased convective heat transfer. At $\theta_w = 1$ (identical temperatures in both regions) and a rising Biot number at the upper disc parameter D, convective heat transfer at the upper disc surface becomes more important than internal heat conduction within the solid. This improvement in convective heat transmission results in more effective heat removal from the upper disc. As a result, the upper disk's temperature profiles decline. The convective heat transfer method effectively transports heat away from the upper disk's surface, resulting in a decrease in temperature. Because the lower disk's temperature is the same as the top disk's initial temperature, it is unaffected. At $\theta_w = 1.5$ (temperature difference between sections) and a rising Biot number at the upper disc parameter D, convective heat transfer at the upper disk's surface is intensified in comparison to internal heat conduction within the solid. Because of the increased convective heat transfer, the temperature profiles of the upper disc decline more quickly. Because the temperature of the upper disc is higher than that of the lower disc, the convective process successfully transports heat away from the upper disc, causing its temperature to fall. The temperature of the lower disc is virtually unaffected since it remains constant or is altered to a lesser extent. The fundamental component in both circumstances is the dominance of convective heat transfer over internal heat conduction. An increase in the Biot number at the upper disc parameter D results in stronger convective heat transport from the upper disk's surface, resulting in a fall in its temperature profiles.

Figure 13 indicates the impact of heat sink/source parameter Q on the nondimensional temperature distribution. Temperature profiles often increase as the heat sink/source

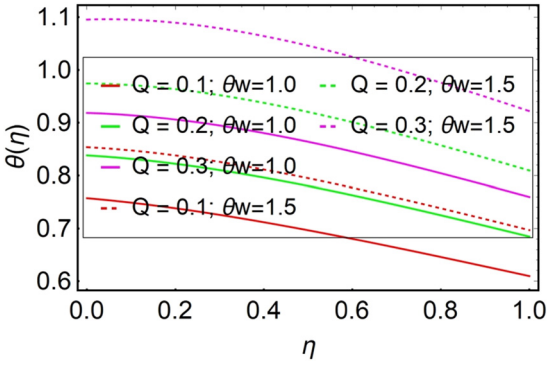

Figure 13: Influence of Q and θ_w on $\theta(\eta)$.

parameter Q increases in stretchy rotatory discs at both $\theta_w = 1$ and $\theta_w = 1.5$. This is because increasing the heat sink/source parameter Q causes more heat to be added from the system, affecting the overall temperature distribution inside the discs. A rise in the heat source parameter Q indicates that more heat is being introduced into the system. This additional heat input increases the thermal energy within the discs, causing them to heat up. Furthermore, the direct input of thermal energy to the fluid, increased internal heat generation, and the positive source term in the energy balance equation all contribute to the fluid's temperature increase as the heat source parameter rises. Higher overall temperatures are achieved inside the fluid domain as a result of this shifting of the thermal equilibrium. The heat source helps to raise the temperature profiles in the top and lower discs.

Figure 14 illustrates the impact of magnetic parameter M on the nondimensional temperature distribution. Temperature profiles tend to grow in stretchy rotatory discs as the magnetic parameter M increases for both $\theta_w = 1$ and $\theta_w = 1.5$. This behavior is caused by the magnetic field's influence on heat transfer and fluid dynamics within the system. A greater magnetic field within the system correlates with an increase in the magnetic parameter M. This magnetic field has the potential to influence fluid flow patterns and heat transfer rates. Heat transport is frequently boosted in the presence of a magnetic field due to changes in the convective and conductive processes. Furthermore, the fluid's temperature rises with a rise in the magnetic parameter because of increased viscous dissipation, Joule heating, and changes in the flow structure brought about by the Lorentz force.

Figure 15 indicates the influence of Eckert number Ec on the nondimensional temperature distribution. Temperature profiles tend to increase in stretchy rotatory discs as the Eckert number (Ec) increases for both $\theta_w = 1$ and $\theta_w = 1.5$. The Eckert number is a dimensionless metric that

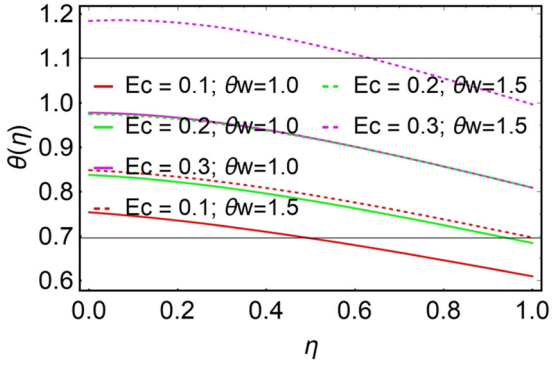

Figure 15: Influence of Ec and θ_w on $\theta(\eta)$.

characterizes the balance of kinetic and thermal energy in a fluid flow by representing the ratio of kinetic energy change to enthalpy change. A rise in the Eckert number suggests that there is more kinetic energy present than enthalpy change. This increased kinetic energy can improve heat mixing and transfer throughout the fluid. In other words, a higher Eckert number indicates that the fluid flow's kinetic energy has a greater impact on the entire heat transfer process. Moreover, the temperature rises with the growing Eckert number due to increased convective heat transfer in the fluid flow; this means that there is more kinetic energy available for convective processes to convert into thermal energy, which raises the temperature of the fluid.

Figure 16 indicates the effect of the Radiation parameter Rd on the nondimensional temperature distribution. Temperature profiles tend to grow when the radiation parameter (Rd) in stretchy rotatory discs increases for both $\theta_w = 1$ and $\theta_w = 1.5$. This is because of the effect of radiative heat transfer on the overall thermal energy distribution within the system. Radiative heat transfer becomes more prevalent in the overall heat transfer process as the radiation parameter Rd grows. Radiative heat transfer is less impacted by fluid characteristics and may transport heat over greater

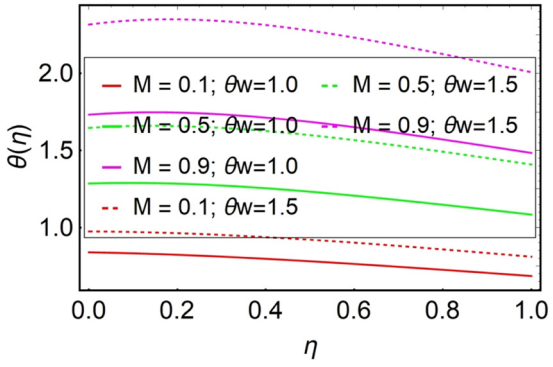

Figure 14: Influence of M and θ_w on $\theta(\eta)$.

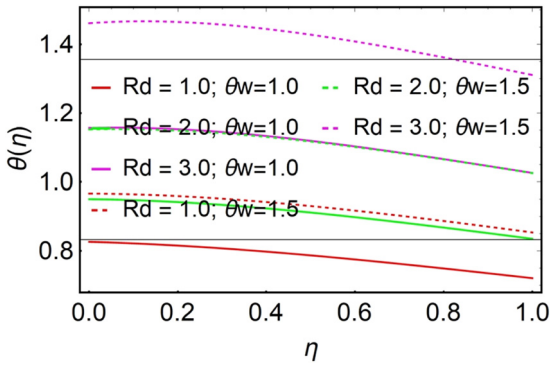

Figure 16: Influence of Rd and θ_w on $\theta(\eta)$.

distances, making it especially important in systems with substantial temperature differences.

4.3 Skin friction and local Nusselt number

Table 4 indicates the influence of skin friction for numerous values of We, M, A, B, and Ω. From Table 4, we observe that an increase in the Weissenberg number (We) may result in a drop in skin friction coefficients for a shear-thinning fluid (n = 0.5) that becomes less viscous with increasing shear rate. This is because a larger Weissenberg number shows that elastic effects have a greater influence on flow behavior. The elasticity of the fluid increases as the Weissenberg number increases. Higher elasticity in this instance could result in the fluid's capacity to restore its shape more effectively following deformation. This has the ability to minimize shear stress and, as a result, skin friction on a solid surface. The influence of the Weissenberg number on skin friction coefficients may differ for a shear-thickening fluid (n = 1.5), which gets more viscous with the increasing shear rate. The elastic effects become more evident as the Weissenberg number increases, potentially resulting in increased shear stresses and skin friction. Increased Weissenberg number may result in increased deformation resistance and a tendency for the fluid to "stick" to the surface, resulting in increased friction along both the radial and azimuthal axes.

Table 4 also indicates that when the magnetic parameter M increases then the skin friction along the redial and azimuthal direction grows because, as the magnetic parameter (M) grows, so does the magnetic field's influence on fluid velocity. The magnetic field can cause Lorentz forces to change the flow pattern, thus increasing resistance to motion. In this instance, the magnetic field may obstruct fluid flow in both the radial and azimuthal directions, leading to higher skin friction coefficients.

Table 4 indicates that when the stretching parameters A and B are increased, the discs are stretched more. This increased stretching might result in improved fluid motion and higher shear rates. Higher shear rates can result in lower apparent viscosity in shear-thinning and shear-thickening fluids. As a result, the flow resistance and skin friction coefficients may drop.

In Table 4, we see that when the rotational parameter increases in the radial direction, it often leads to higher angular velocities, which might result in increased centrifugal forces. Higher shear rates can cause a drop in apparent viscosity in the case of a shear-thinning fluid (n = 0.5). This decrease in viscosity reduces flow resistance, resulting in reduced radial skin friction coefficients. Higher shear rates can cause an increase in apparent viscosity in the case of a shear-thickening fluid (n = 1.5). This increased viscosity increases flow resistance, resulting in larger radial skin friction coefficients. Increases in the rotational parameter in the azimuthal direction frequently result in more fluid motion and higher angular velocities. Increased mobility might result in more aggressive mixing and higher shear rates. Higher shear rates can cause variations in apparent viscosity in both shear-thinning (n = 0.5) and shear-thickening (n = 1.5) fluids. The viscosity of shear-thinning fluids may decrease, thus reducing resistance and leading to reduced skin friction

Table 4: Numerical outcomes of skin friction coefficients in radial and azimuthal directions for change values of We, M, A, B, Ω

We	M	A	B	Ω	$\mathrm{Re}^{\frac{1}{2}}\mathrm{C}_{\mathrm{Fr}}$		$\mathrm{Re}^{\frac{1}{2}}\mathrm{C}_{G\theta^*}$	
					n = 0.5	n = 1.5	n = 0.5	n = 1.5
0.1	0.1	0.1	0.1	0.1	0.463546	0.486463	0.323567	0.335425
0.4					0.444567	0.469866	0.318643	0.328646
0.7					0.430023	0.440754	0.309753	0.314678
0.1	0.2				0.696537	0.756864	0.213674	0.243567
	0.6				0.705336	0.765357	0.235885	0.268975
	1.2				0.713466	0.775319	0.249075	0.287523
	0.1	0.1			0.697647	0.895458	0.298654	0.375367
		0.2			0.680963	0.885436	0.287633	0.368775
		0.3			0.678537	0.875421	0.275327	0.357543
		0.1	0.1		0.457906	0.557547	0.254364	0.397635
			0.2		0.435685	0.540862	0.236853	0.389863
			0.3		0.424614	0.537995	0.219985	0.369949
			0.1	0.2	0.544263	0.676467	0.356786	0.487554
				0.3	0.557754	0.665374	0.368933	0.497527
				0.4	0.564336	0.654356	0.375658	0.510096

coefficients. The viscosity of shear-thickening fluids may increase, potentially leading to increased resistance and skin friction coefficients.

Table 4 illustrates the influence of the Nusselt number for different numbers of Rd, Ec, M, C, and D. Increasing the radiation parameter, Eckert number, magnetic parameter, and Biot number at both the bottom and upper discs improve convective heat transmission and fluid mixing, according to Table 4. Higher Nusselt numbers result from enhanced convective heat transfer for both $\theta_w = 1$ and $\theta_w = 1.5$. Increasing the radiation parameter (Rd) frequently improves radiative heat transfer. This new heat transfer mechanism boosts the convective heat transfer component, resulting in higher Nusselt numbers for both $\theta_w = 1$ and $\theta_w = 1.5$. Increased radiative heat transfer provides a more efficient heat exchange process, which results in higher Nu. The Eckert number (Ec) connects the change in kinetic energy to the change in enthalpy in fluid flow. An increase in Ec can improve kinetic energy, resulting in more vigorous fluid mixing and better heat transmission. This increases convective heat transfer and, as a result, Nusselt values for both $\theta_w = 1$ and $\theta_w = 1.5$. The magnetic parameter (M) increases the magnetic field's influence on fluid velocity. This improves convective mixing and heat transport, resulting in greater Nusselt numbers for $\theta_w = 1$ and $\theta_w = 1.5$. The interaction of the magnetic field with the fluid can change flow patterns and promote more effective heat exchange. The ratio of convective heat transfer at the surface to conductive heat transfer within the material is represented by the Biot number. The greater the Biot number, the greater the contribution of convective heat transfer. This improves heat exchange between the fluid and the discs, resulting in greater Nusselt numbers for $\theta_w = 1$ and $\theta_w = 1.5$ (Table 5).

Table 5: Numerical outcomes of Nusselt number coefficients for change in values of Rd, Ec, M, C, D

Rd	Ec	M	C	D	$\mathbf{Re}^{-\frac{1}{2}}\mathbf{Nu_r}$	
					$\theta_w = 1.0$	$\theta_w = 1.5$
0.1	0.1	0.1	0.1	0.1	0.555472	0.657757
0.2					0.586473	0.697853
0.3					0.609967	0.734578
0.1	0.2				0.546784	0.567853
	0.3				0.554383	0.578653
	1.4				0.569076	0.588595
	0.1	0.1			0.497654	0.556848
		0.2			0.507543	0.567896
		0.3			0.514952	0.579087
		0.1	0.1		0.690758	0.887646
			0.2		0.747856	0.946785
			0.3		0.896528	0.999963
			0.1	0.2	0.577973	0.698658
				0.3	0.608743	0.747996
				0.4	0.636795	0.804474

5 Concluding remarks

In this work, we analyzed the consequences of convective heat transport in the MHD flow of Carreau HNF between two disks that are rotating as well as stretching. The Tiwari and Das nanofluid model is employed to model the fluid flow dynamics in terms of PDEs by taking into account the thermal radiation, viscous dissipation, joule heating, and heat generation/absorption. The resultant PDEs are then transmuted into ODEs by defining appropriate similarity variables. The converted complex ODEs are then solved by HAM passed through MATLAB. The significant outcomes of the current analysis are as follows:

- When the stretching parameter at the bottom disc A and at the upper disc B of a stretchy rotatory disc rises, the fluid velocity profiles alter for $n = 0.5$ and $n = 1.5$. Radial expansion causes greater speeds in the radial direction, whereas azimuthal contraction causes lower velocities in the azimuthal direction.
- Increases in the rotation parameter of stretchy rotatory discs result in increased radial and azimuthal velocities for both $n = 0.5$ and $n = 1.5$.
- For both $n = 0.5$ and $n = 1.5$, increases in the magnetic parameter produce decreases in radial and azimuthal velocities in stretchy rotatory discs due to higher magnetic forces restricting fluid motion.
- The temperature profile increases at $\theta_w = 1$ and decreases at $\theta_w = 1.5$ when the Biot number at lower disc C increases.
- The temperature profile decreases at both $\theta_w = 1$ and $\theta_w = 1.5$ when the Biot number at the upper disc D increases.
- The temperature profile increases at both $\theta_w = 1$ and $\theta_w = 1.5$ when the heat source/sink parameter, magnetic parameter, Eckert number, and radiation parameter increase.
- The skin friction coefficient decreases for both radial and azimuthal directions at $n = 0.5$ and $n = 1.5$ as the Weissenberg number and the stretching parameters at both the lower and upper discs increase.
- The skin friction coefficient increases for both radial and azimuthal directions at $n = 0.5$ and $n = 1.5$ as the magnetic parameter increases.
- For $n = 0.5$, the skin friction coefficients increase in the radial direction as the rotational parameter increases,

while for $n = 1.5$, they decrease. Conversely, in the azimuthal direction, skin friction coefficients increase for both $n = 0.5$ and $n = 1.5$ as the rotational parameter increases.

- Raising the radiation parameter, Eckert number, magnetic parameter, and Biot number at both the bottom and upper discs improves the Nusselt numbers for both $\theta_w = 1$ and $\theta_w = 1.5$.

6 Future research direction

In the future, the current study can be extended by considering entropy generation in ternary hybrid nanoparticles over various plane and rough surfaces in the presence of various physical effects such as stagnation point flow, porous medium, bioconvection, and activation energy subject to slip and convective-Nield boundary conditions.

Acknowledgments: This project was supported by Researchers Supporting Project number (RSP2024R411), King Saud University, Riyadh, Saudi Arabia.

Funding information: The project was financed by Lucian Blaga University of Sibiu through research grant LBUS – IRG – 2023 – 09.

Author contributions: All authors have accepted responsibility for the entire content of this manuscript and approved its submission.

Conflict of interest: The authors state no conflict of interest.

Data availability statement: The datasets generated and/or analyzed during the current study are available from the corresponding author on reasonable request.

References

[1] Kármán TV. Über laminare und turbulente Reibung. ZAMM - J Appl Math Mech/Z Angew Math Mech. Jan. 1921;1(4):233–52. doi: 10.1002/ZAMM.19210010401.

[2] Fang T, Zhang J. Flow between two stretchable disks – An exact solution of the Navier–Stokes equations. Int Commun Heat Mass Transf. Oct. 2008;35(8):892–5. doi: 10.1016/J.ICHEATMASSTRANSFER.2008.04.018.

[3] Imtiaz M, Hayat T, Alsaedi A, Ahmad B. Convective flow of carbon nanotubes between rotating stretchable disks with thermal radiation effects. Int J Heat Mass Transf. Oct. 2016;101:948–57. doi: 10.1016/J.IJHEATMASSTRANSFER.2016.05.114.

[4] Ahmed J, Khan M, Ahmad L. MHD swirling flow and heat transfer in Maxwell fluid driven by two coaxially rotating disks with variable thermal conductivity. Chin J Phys. Aug. 2019;60:22–34. doi: 10.1016/J.CJPH.2019.02.010.

[5] Usman U, Ghaffari A, Kausar S. Numerical solution of the partial differential equations that model the steady three-dimensional flow and heat transfer of Carreau fluid between two stretchable rotatory disks. Numer Methods Partial Differ Equ. Sep. 2023;39(5):3532–60. doi: 10.1002/NUM.22672.

[6] Usman, Ghaffari A, Muhammad T, Mustafa I. Heat transfer enhancement in a power-law nanofluid flow between two rotating stretchable disks. Pramana - J Phys. Mar. 2022;96(1):1–11. doi: 10.1007/S12043-021-02272-0/METRICS.

[7] Das S, Ali A. Dynamical phenomena developed by a spiralling stretchable sheet in magnetized Casson-spinel ferrite nanofluid. Heliyon. Aug. 2023;9:e18376. doi: 10.1016/j.heliyon.2023.e18376.

[8] Das S, Das S. EDL Aspects in swirling ionic tribological fluid flow in a squeezed/split channel underlie a high-power magnetic field. Forces Mech. May. 2023;11:100196. doi: 10.1016/j.finmec.2023.100196.

[9] Yashkun U, Zaimi K, Abu Bakar NA, Ishak A, Pop I. MHD hybrid nanofluid flow over a permeable stretching/shrinking sheet with thermal radiation effect. Int J Numer Methods Heat Fluid Flow. 2021;31(3):1014–31.

[10] Lund LA, Yashkun U, Shah NA. Multiple solutions of unsteady Darcy–Forchheimer porous medium flow of Cu–Al_2O_3/water based hybrid nanofluid with joule heating and viscous dissipation effect. J Therm Anal Calorim. 2024;149:2303–15.

[11] Waini I, Ishak A, Pop I. Flow and heat transfer of a hybrid nanofluid past a permeable moving surface. Chin J Phys. Aug. 2020;66:606–19. doi: 10.1016/J.CJPH.2020.04.024.

[12] Zainal NA, Nazar R, Naganthran K, Pop I. MHD mixed convection stagnation point flow of a hybrid nanofluid past a vertical flat plate with convective boundary condition. Chin J Phys. Aug. 2020;66:630–44. doi: 10.1016/J.CJPH.2020.03.022.

[13] Waini I, Ishak A, Groşan T, Pop I. Mixed convection of a hybrid nanofluid flow along a vertical surface embedded in a porous medium. Int Commun Heat Mass Transf. May 2020;114:104565. doi: 10.1016/J.ICHEATMASSTRANSFER.2020.104565.

[14] Rostami MN, Dinarvand S, Pop I. Dual solutions for mixed convective stagnation-point flow of an aqueous silica–alumina hybrid nanofluid. Chin J Phys. Oct. 2018;56(5):2465–78. doi: 10.1016/J.CJPH.2018.06.013.

[15] Shamshuddin MD, Saeed A, Asogwa KK, Jamshed W. A semi-analytical approach to investigate the entropy generation in a tangent hyperbolic magnetized hybrid nanofluid flow upon a stretchable rotating disk. J Magn Magn Mater. May 2023;574:170664. doi: 10.1016/J.JMMM.2023.170664.

[16] Farooq U, Imran M, Fatima N, Noreen S, Tahir M, Akgül A, et al. Cattaneo-Christov heat flux model in radiative flow of (Fe3O4–TiO_2/Transformer oil) and (Cu–TiO_2/Transformer oil) magnetized hybrid nanofluids past through double rotating disks. Case Stud Therm Eng. May 2023;45:102905. doi: 10.1016/J.CSITE.2023.102905.

[17] Agrawal R, Kaswan P. Entropy generation minimization of Ag-Fe_3O_4/water-ethylene glycol squeezed hybrid nanofluid flow between parallel disks . Int J Numer Methods Heat Fluid Flow. Jan. 2023;33(1):65–95. doi: 10.1108/HFF-01-2022-0005/FULL/XML.

[18] Waini I, Ishak A, Pop I. Unsteady flow and heat transfer past a stretching/shrinking sheet in a hybrid nanofluid. Int J Heat Mass

Transf. Jun. 2019;136:288–97. doi: 10.1016/J.IJHEATMASSTRANSFER.2019.02.101.

[19] Khashi'ie NS, Arifin NM, Pop I, Nazar R, Hafidzuddin EH, Wahi N. Three-dimensional hybrid nanofluid flow and heat transfer past a permeable stretching/shrinking sheet with velocity slip and convective condition. Chin J Phys. Aug. 2020;66:157–71. doi: 10.1016/J.CJPH.2020.03.032.

[20] Anuar NS, Bachok N, Pop I. Influence of buoyancy force on Ag-MgO/water hybrid nanofluid flow in an inclined permeable stretching/shrinking sheet. Int Commun Heat Mass Transf. Apr. 2021;123:105236. doi: 10.1016/J.ICHEATMASSTRANSFER.2021.105236.

[21] Rooman M, Jan MA, Shah Z, Vrinceanu N. Entropy optimization on axisymmetric darcy-forchheimer powell-eyring nanofluid over a horizontally stretching cylinder with viscous dissipation effect. Coatings. May 2022;12(6):749. doi: 10.3390/COATINGS12060749.

[22] Rooman M, Jan MA, Shah Z, Alzahrani MR. Entropy generation and nonlinear thermal radiation analysis on axisymmetric MHD Ellis nanofluid over a horizontally permeable stretching cylinder. Waves Random Complex Media. 2022;1–15. doi: 10.1080/17455030.2021.2020934.

[23] Shutaywi M, Rooman M, Jan MA, Vrinceanu N, Shah Z, Deebani W. Entropy generation and thermal analysis on MHD second-grade fluid with variable thermophysical properties over a stratified permeable surface of paraboloid revolution. ACS Omega. Aug. 2022;7(31):27436–49. doi: 10.1021/ACSOMEGA.2C02452.

[24] Carreau PJ. Rheological equations from molecular network theories. Trans Soc Rheol. Mar. 1972;16(1):99–127. doi: 10.1122/1.549276.

[25] Sulochana C, Ashwinkumar GP, Sandeep N. Transpiration effect on stagnation-point flow of a Carreau nanofluid in the presence of thermophoresis and Brownian motion. Alex Eng J. Jun. 2016;55(2):1151–7. doi: 10.1016/J.AEJ.2016.03.031.

[26] Khan M, Irfan M, Khan WA, Alshomrani AS. A new modeling for 3D Carreau fluid flow considering nonlinear thermal radiation. Results Phys. Jan. 2017;7:2692–704. doi: 10.1016/J.RINP.2017.07.024.

[27] Irfan M, Khan M, Khan WA. Numerical analysis of unsteady 3D flow of Carreau nanofluid with variable thermal conductivity and heat source/sink. Results Phys. Jan. 2017;7:3315–24. doi: 10.1016/J.RINP.2017.08.029.

[28] Rooman M, Shah Z, Bonyah E, Jan MA, Deebani W. Mathematical modeling of Carreau fluid flow and heat transfer characteristics in the renal tubule. J Math. May. 2022;2022:2517933. doi: 10.1155/2022/2517933.

[29] Abbas IA. Generalized thermoelastic interaction in functional graded material with fractional order three-phase lag heat transfer. J Central South Univ. May. 2015;22(5):1606–13. doi: 10.1007/s11771-015-2677-5.

[30] Abbas I, Hobiny A, Marin M. Photo-thermal interactions in a semiconductor material with cylindrical cavities and variable thermal conductivity. J Taibah Univ Sci. Sept. 2020;14(1):1369–76. doi: 10.1080/16583655.2020.1824465.

[31] Marin M, Hobiny A, Abbas I. The effects of fractional time derivatives in porothermoelastic materials using finite element method. Mathematics. June 2021;9(14):1606. doi: 10.1080/16583655.2020.1824465.

[32] Takabi B, Salehi S. Augmentation of the heat transfer performance of a sinusoidal corrugated enclosure by employing hybrid nanofluid. Adv Mech Eng. Jan. 2014;6:147059. doi: 10.1155/2014/147059.

[33] Lone SA, Shamshuddin MD, Shahab S, Iftikhar S, Saeed A, Galal AM. Computational analysis of MHD driven bioconvective flow of hybrid Casson nanofluid past a permeable exponential stretching sheet with thermophoresis and Brownian motion effects. J Magn Magn Mater. Aug. 2023;580:170959. doi: 10.1016/J.JMMM.2023.170959.

[34] Irfan M, Khan M, Khan WA. Interaction between chemical species and generalized Fourier's law on 3D flow of Carreau fluid with variable thermal conductivity and heat sink/source: A numerical approach. Results Phys. Sep. 2018;10:107–17. doi: 10.1016/J.RINP.2018.04.036.